Chapter 4

Cathodic corrosion induced selective nano-crystallization of Nickel oxo/hydroxo complex on (NiFeCr)SiB amorphous ribbon for Alkaline Oxygen evolution reaction and Methanol oxidation reaction

4.1. Introduction

This study highlights the importance of the chemical composition of Ni-amorphous alloy and surface re-construction techniques to improve the catalytic performance. In this present work, a novel $(Ni_{87}Fe_4Cr_9)_{78}Si_8B_{14}$ amorphous alloy ribbon is considered and different proportions of α-$Ni(OH)_2$ are synthesized in-situ on the ribbon surface through potentiostatic cathodic corrosion, applied for varied times (30, 45, 60, 90 and 120 minutes). Corroded ribbon samples are investigated as electro-catalysts in presence of 1 M KOH and 1 M KOH + 1 M MeOH respectively, for OER and MOR studies. This work highlights the application of amorphous ribbons and their surface-corroded counterparts as self-supported up-scalable electro-catalyst for OER and MOR. While previous studies have explored Ni-based amorphous alloys for OER applications, to the best of our knowledge, this is the first report demonstrating the potential of such materials for MOR. The findings underscore the versatility of amorphous alloys in electro-catalysis and introduce a new class of materials for direct methanol fuel cell (DMFC) applications.

4.2. Preparation of Ni-amorphous precursor ribbons through melt-spinning

The master alloy of nominal composition $(Ni_{87}Fe_4Cr_9)_{78}Si_8B_{14}$ was produced using high purity elements through inert arc-melting technique. The master alloy ingots were re-melted multiple times to ensure thorough homogenization of the alloy. Subsequently, the prepared alloy ingot is induction melted and the molten metal is poured over a rotating cooling drum to obtain a continuous wide ribbon of 25 mm width and average ribbon thickness of ~28 µm. The melt-spun ribbons are bendable and exhibit metallic lustre.

4.3. Surface modification of precursor melt-spun ribbon

The precursor ribbons were cut into rectangular samples with a cross-sectional area of 20 x 10 mm^2 and then underwent surface modification through potentiostatic cathodic corrosion to create electrochemically active surface phases [66]. The chrono-amperometric method for the corrosion of the ribbon surface was carried out in a 1 M KOH electrolyte at a potential corresponding to 10 mA/cm^2 (hydrogen generation regime) with a scan rate of 20 mV s^{-1} (**Fig. S1**). To study the impact of corrosion time on catalytic performance, the corrosion duration was systematically varied to 0, 30, 45, 60, 90, and 120 minutes, respectively. The samples are labelled as S0, S30, S45, S60, S90, and S120 to indicate the different modification times used in this study. These corroded ribbon electrodes were thoroughly washed with deionized water, ethanol, and dried at room temperature. The modified ribbons were then used in subsequent OER and MOR experiments.

4.4. Electrochemical performance

The OER and MOR experiments were conducted using a three-electrode electrochemical workstation (Admiral Instrument, USA) using 1 M KOH and 1 M KOH + 1 M MeOH

electrolytes, respectively. The Hg/HgO was used as the reference electrode, ribbon samples act as working electrode and graphite was used for the counter electrode. Apart from the ribbon samples, RuO_2 loaded (8mg/cm^2) NF samples were also tested for OER to benchmark the performance. Using the Nernst equation, the polarization curves obtained with respect to Hg/HgO electrode were converted to reversible hydrogen electrode (RHE) through the relation $\boldsymbol{E_{RHE} = E_{Hg/HgO} + 0.0591 \times pH + 0.098}$. Similarly, the over-potential for OER was calculated by $\eta = \boldsymbol{E_{RHE} - 1.23}$.

The scan rate was increased from 10, 20, 50, 100, 150, and 200 mV s^{-1} to capture cyclic voltammetry (CV) and linear sweep voltammetry (LSV) in 1 M KOH solution both in the presence as well in absence of 1 M MeOH. Response recorded for 20 mV s^{-1} are considered for comparison. The measurements of electrochemical impedance spectroscopy (EIS) were performed with an AC perturbation of 10 mV between the frequency range of 100 kHz to 0.1 Hz, with 1 M KOH in both the presence as well in absence of 1 M MeOH. Turnover Frequency (TOF) was calculated using the number of electrochemically active sites with the back sweep of cyclic voltammetry curve measured at 500 mV s^{-1}, using following equation.

$$\boldsymbol{TOF = (J \times NA)/(n \times F \times \Gamma)} \qquad \text{---------- (1)}$$

Where J, NA, n, F represents the value of current density at vertex potential, Avogadro′s number, number of electrons transfer and Faraday constant respectively. Value of Γ represents the number of electrochemically accessible sites obtained from the peak area of the backward sweep. The double-layer capacitances (C_{dl}) were acquired by performing cyclic voltammetry at different scan rate in a non-faradic region. Electrochemical active surface area (ECSA) calculated using the equation ECSA = C_{dl}/C_s, where Cs represents

the specific capacitance. The C_s value was considered as 0.04 $mF.cm^{-2}$ based on the previous studies [50]. The stability test was performed in 1 M KOH solution both in presence as well in absence of 1 M MeOH, respectively, at 1.5 V and 1.7 V vs RHE, for 8 hours. All electrochemical data are iR compensated for 80%.

4.5. Results and Discussion

4.5.1 Structural and Phase analysis of surface modified ribbons

Figure 4.1a displays the XRD patterns obtained from the surface of melt-spun precursor (S0) and cathodic corroded ribbons samples (S30 - S120). The XRD pattern of melt-spun ribbon (S0) depicts diffuse halo broad region between 37.5° to 55° indicating the complete amorphous nature of the ribbons. However, all the ribbons subjected to surface modification (S30 - S120) depicts additional broad peaks at 22.5° indicating generation of new crystal phase on the ribbon surface. Moreover, the observed crystal peak broadening and integral intensity varies from 30 min to 120 min, highlighting the strong correlation between the generated crystal phase and the corrosion time. To understand the crystallographic details, a slow XRD scan carried out from lower 2θ region between 5° - 70° for S45 and S60 samples as shown in **Figure 4.1b**.

The crystallographic peak analysis confirms the occurrence of monoclinic α-$Ni(OH)_2$ phase (ICSD PDF No: 00-041-1424) and relatively minor presence of monoclinic hydrated Nickel carbonate, $NiCO_3.6H_2O$ (ICSD PDF No: 00-012-0276). In the presence of OH^- ions (1 M KOH), $Ni(OH)_2$ gets deposited on the surface of the ribbon. The alkaline electrolyte (1 M KOH) preferably solubilizes the atmospheric CO_2, which leads to the formation of carbonate anions (CO_3^{2-}). These carbonate ions (relatively lower concentration than OH^-) combined with the Ni^{2+} to form low concentration of nickel carbonate ($NiCO_3.6H_2O$) phase. Moreover, the XRD slow scan reveals two observations

namely, (i) presence of broader asymmetric peak region between 14.6° to 16.8° and (ii) the relative XRD peak intensity and broadening of (006) is much higher than (003) peak (**Figure 4.1c-d)**. The observation corroborates the "turbostratic" disorder nature of α-$Ni(OH)_2$ .x H_2O phase, wherein different degree of hydration between the c-axis planes of (003) and (006) varies the peak behaviour [53]. Also, the (006) peak feature manifests the existence of textured crystallization of nano α-$Ni(OH)_2$ phase on the ribbon surface during the cathodic corrosion.

To quantitatively assess the evolution of α-$Ni(OH)_2$ phase features with cathodic corrosion time, the peak broadening (FWHM) and integral area of (0 0 6) peak is calculated through peak fitting. It is evident that the both integral peak area representing the volume fraction of α-$Ni(OH)_2$ and FWHM representing the nano-structuring of the crystals shows cyclical trend with increasing time. With the increase of cathodic corrosion time , the volume fraction of α-$Ni(OH)_2$ generated reaches a maximum for S60 and decreases gradually for extended corrosion time. Similarly, the FWHM of the peak indicates the presence of nanostructured α-$Ni(OH)_2$ in the range of 3.5-7 nm. The XRD study confirms the electrochemical activation of Ni amorphous ribbon surface to form α-$Ni(OH)_2$ phase, preferable for electrocatalytic activity [97]. It is noteworthy to mention, similar surface activation of Ni based metallic surface yields β-$Ni(OH)_2$, whereas the present precursor yields electrochemically superior α-$Ni(OH)_2$.

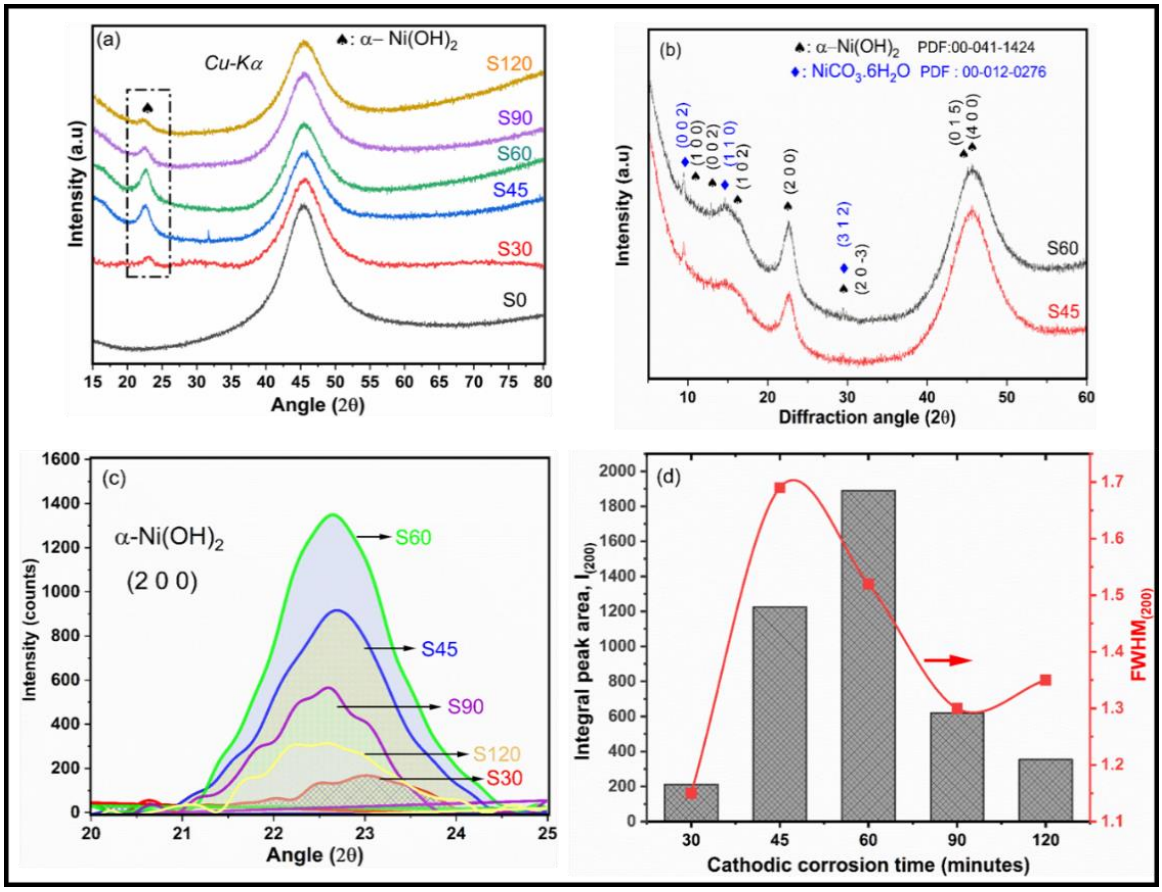

Figure 4.1- (a) XRD patterns of melt-spun (S0) and surface modified samples S30, S45, S60, S90 and S120. (b) XRD slow scan pattern for S45 and S60 samples. (c) Peak intensity curves for S30, S45, S60, S90 and S120 samples indicating (2 0 0) plane of α-$Ni(OH)_2$. (d) Effect of corrosion time on Integral peak area and FWHM of (2 0 0) plane.

Further, the TEM micrographs and SAED patterns were obtained to confirm the crystallization of nano α-$Ni(OH)_2$ phase on the amorphous ribbon surface (**Figure 4.2a-e**). The bright field (BF) image of S0 (melt-spun) ribbon show single-phase region, lacking any microstructural features representing the amorphous nature. The corresponding SAED pattern shows only the presence of broad ring confirming the complete amorphous nature of the ribbons. Whereas, the BF TEM image of S60 sample clearly shows the distribution of nanostructured crystal phase (9.4 ± 1.3 nm) in the

amorphous matrix. Further the corresponding SAED pattern substantiates the combination of crystal spot pattern along with broad ring pattern.

The indexing of the diffraction spot pattern reveals the presence of (101), (012), (015), (110), and (113) crystallographic planes corresponding to α-$Ni(OH)_2$ [53,98]. Moreover, an off-axis illumination of (101) spot brightens the α-$Ni(OH)_2$ nanoparticles as shown in the dark-field image. The TEM results validate the morphology, size, and crystallography of α-$Ni(OH)_2$ particles and in agreement with the XRD results.

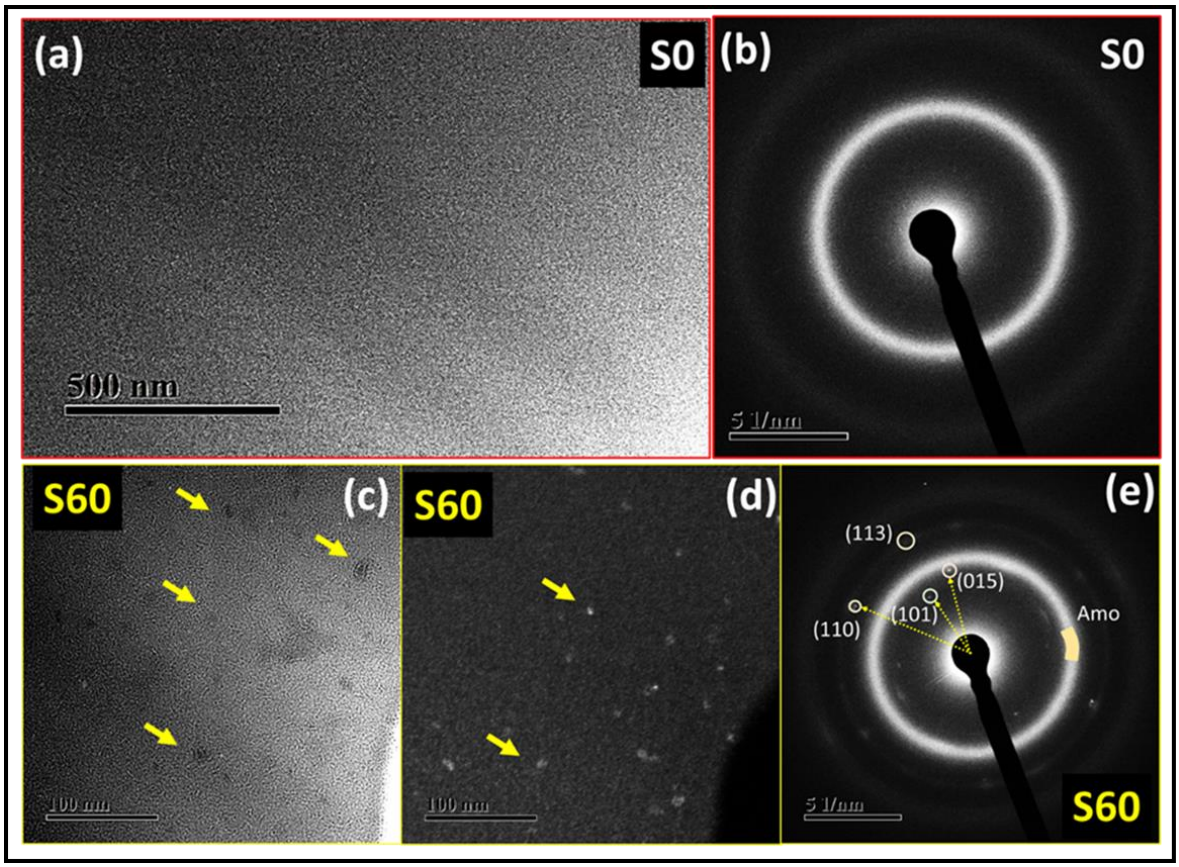

Figure 4.2- The TEM (a) SAED (b) patterns of melt-spun amorphous ribbon (S0) sample. The bright-field (c), dark-field (d), and SAED patterns of surface modified S60 sample depicting the crystallization of nano α-$Ni(OH)_2$ phase in the amorphous ribbon.

4.5.2 Morphology and Compositional analysis

To understand the occurrence, distribution, size and morphology of the activated α-$Ni(OH)_2$ phase, SEM studies were conducted on the cathodic corroded samples with different holding time (**Figure 4.3a-f**). The backscattered SEM image of melt-spun ribbon (S0) surface show plain surface features. Whereas, the surface etched samples shows varying distribution of nano-sized α-$Ni(OH)_2$ (white regions) phase. The size and distribution of the nano α-$Ni(OH)_2$ are in agreement with the previous XRD results. The volume fraction is highest for S60 ribbon with agglomeration of nanocrystals and subsequent growth via Ostwald ripening phenomenon [99]. With further modification in S90 sample, the hydroxide phases decrease in number density and volume fraction and S120 shows complete dissolution of the hydroxide crystals.

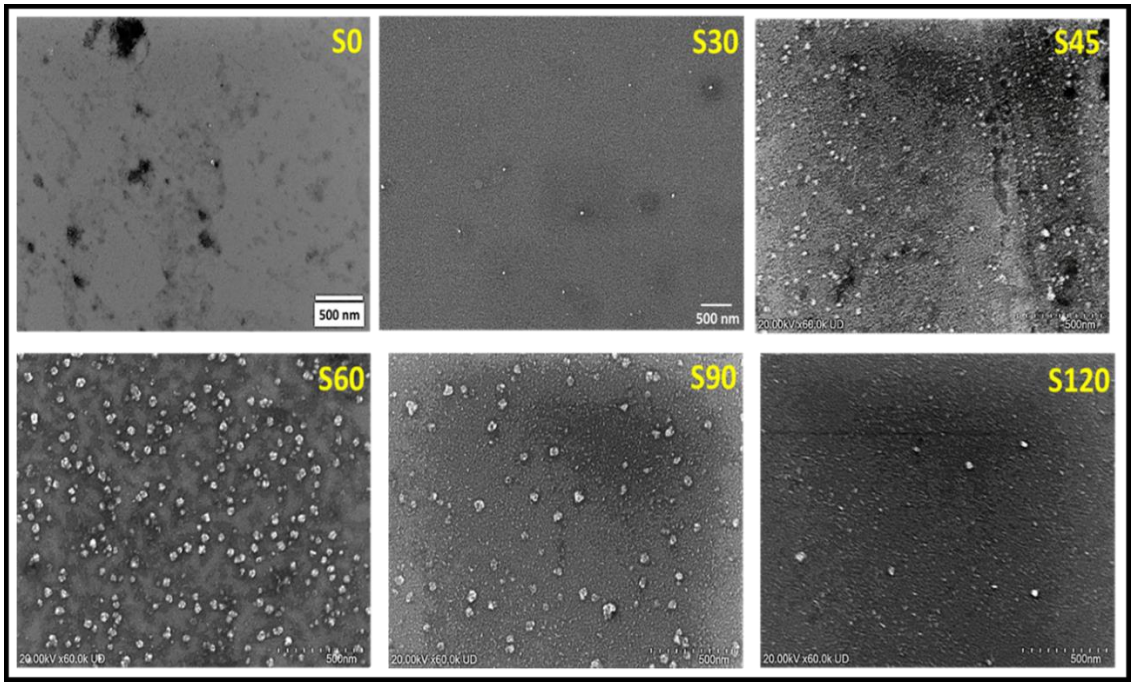

Figure 4.3- (a-f) FESEM images of melt-spun (S0) and surface-modified samples S30, S45, S60, S90 and S120.

To further validate the activated nickel hydroxide crystals, the EDS elemental distribution map of an agglomerated hydroxide region of S60 sample is chosen (**Figure 4.4a-c**). The

elemental mapping clearly reveals distinct chemical elemental re- distribution within and around the vicinity of the hydroxide. The hydroxide (precipitate) exhibits Ni-deficit region with overlapping Fe and O. Whereas ribbon surface region around hydroxide precipitate show enrichment of Ni, and deficit of O. The Cr and Si distribution is uniform as shown in **Figure 4.4a**. The results outline the deficit of nickel with overlapping Fe and O evidencing the presence of $Ni(OH)_2$ with minor substitution of Fe atoms. The EDS area spectra also confirms the chemical re-distribution between ribbon surface and hydroxide mainly Ni and O.

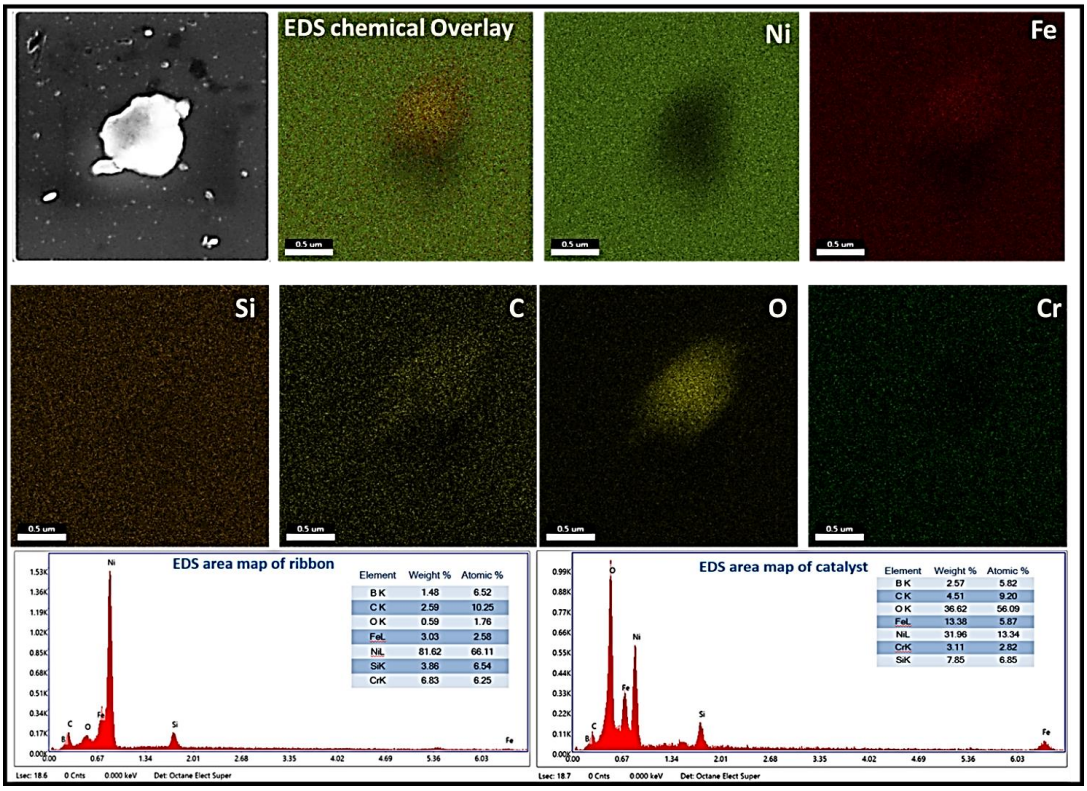

Figure 4.4- (a) EDS elemental mapping results of activated α-$Ni(OH)_2$ crystal depicting combined and individual distribution of Ni, Fe, Si, C, O and Cr and EDS area spectra of (b) ribbon surface and (c) hydroxide.

From the XPS surface survey plot (**Figure 4.5a-d**), the presence of all the elements used in alloy formation is confirmed. It has been also observed that the intensity of O 1s peak is increased after surface treatment. This indicates the generation of oxide or hydroxide or oxy-hydroxide species after surface treatment which enhances the electrochemical performance. To better understand the elemental oxidation state and surface speciation of the elements, core level spectra of Ni 2p and O 1s were performed.

In the S0 sample, Ni $2p_{3/2}$ at 852.9 eV suggests that the surface Ni is predominantly exists in the form of elemental Ni without any significant surface oxidation in amorphous ribbon. Hence, absence of Ni-O type active sites makes the virgin sample less active for electrocatalytic OER and MOR. After surface treatment, the Ni $2p_{3/2}$ peak shifted to higher energy from 852.9 eV to 855.67 eV which suggests that most of the Ni was oxidized to nickel oxide/hydroxide/oxyhydroxide species which acts as active sites for OER/MOR. The deconvoluted Ni $2p_{3/2}$ peak suggests that Ni has been oxidized to NiO, $Ni(OH)_2$ and NiOOH [100].

The formation of the oxygenated species makes the surface-modified ribbon active for OER and MOR. To further confirm the presence of oxygenated species of nickel, core level spectra of O 1s was analysed for S0 and S60 samples. For the S0 sample, the O 1s peak is observed at 532.3 eV, predominantly corresponding to surface adsorbed oxygen. In case of S60 sample, the spectra of O 1s was de-convoluted into three peaks. Peak at 529.8 eV suggest the formation of metal oxide, whereas the peaks at 530.6 eV and 531.5 eV corresponds to the $M(OH)_2$ and MOOH, respectively, preferably for Ni.

The XPS of Fe 2p in figure 4.5d also suggests formation of small fraction of Fe^{3+} and Fe^{2+} after cathodic corrosion. The de-convoluted peaks of Cr 2p is presented in **Fig. S2**. In S0 sample it is observed that Cr is partially oxidized to Cr(III)-O type of compounds

on the ribbon surface. In S60 sample, after surface modification, Cr(III)-OH and Cr(VI)-O are also formed along with Cr(III)-O.

These overall findings further confirmed the generation of oxygenated species on the ribbon surface after surface treatment which makes it more electrocatalytically active [101].

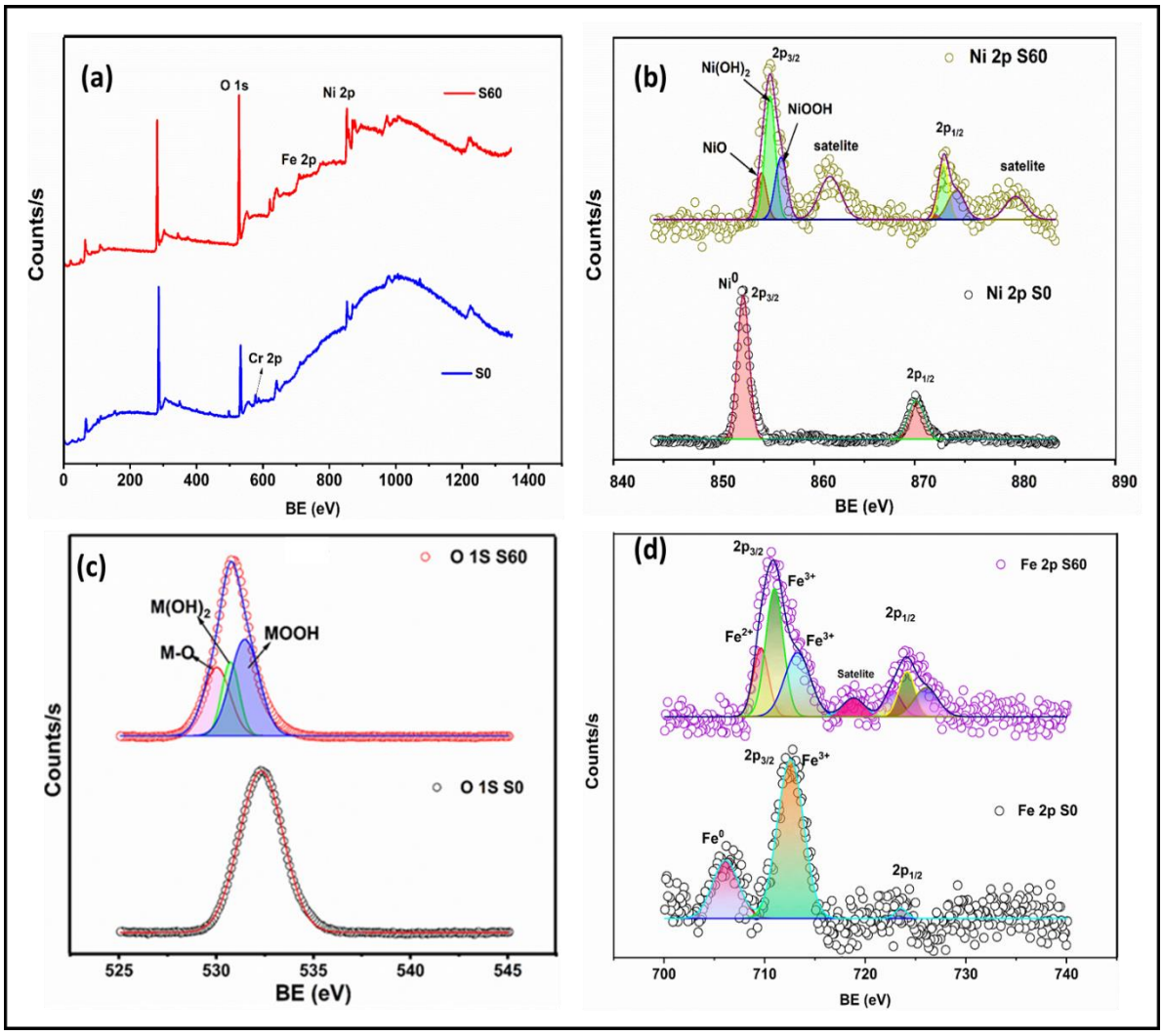

Figure 4.5- XPS spectra of melt-spun (S0) and surface modified (S60) pristine samples (a) Surface scan spectra. (b) Core level spectra of Ni 2p and (c) Core level spectra of O 1s (d) Core level spectra of Fe 2p.

4.5.3 Electrochemical performance

4.5.3.1. OER performance

The electrocatalytic activity of surface-modified ribbons was systematically assessed for OER in 1 M KOH solution. **Figure 4.6a** represents the cyclic voltammetry curve of S60 showing the lowest over-potential of 295 mV at a current density of 10 mA/cm^2, among the investigated S0 (354 mV), S30 (329 mV), S45 (325 mV), S90 (309 mV) and S120 (334 mV) and RuO_2 (270 mV) samples. It has been observed that RuO_2 showed lower over-potential at 10 mA/cm^2 than the ribbon samples but at 100 mA/cm^2 or at higher current density, the surface treated ribbon showed lower over-potential compared to RuO_2. It is evident from **Figure 4.6b** that the over-potential of all modified samples appear to be lower than those of the as spun ribbon, which depicts that the activation energy of the OER reduced significantly.

It is also observed that with the increase in the cathodic corrosion time, the value of over-potential got reduced and observed the minimum value, for one hour (S60) sample and then the value increased further with an increase of time. This may be due to the optimal size of the Ni-oxy/hydroxide formed during surface treatment which gives rise to more activity [102]. The lesser the onset potential, the better is the OER activity and the lesser the electrical losses.

The S60 (1.38 V vs RHE) is found to have lesser onset potential among all surface-modified catalysts, with S0 (1.50 V vs RHE), S30 (1.39 V vs RHE), S45 (1.39 V vs RHE), S90 (1.39 V vs RHE) and S120 (1.40 V vs RHE) studied here. **Figure 4.6c** represents the Tafel slopes of surface- modified samples. S60 presented the lowest Tafel slope value of 51 mV dec^{-1}, which was evidently lesser than the other surface-modified samples with S0 (81.5 mV dec^{-1}), S30 (76 mV dec^{-1}), S45 (66 mV dec^{-1}), S90 (56 mV

dec^{-1}), S120 (56 mV dec^{-1}) and RuO_2 (67 mV dec^{-1}) respectively, indicating the rapid reaction kinetics for S60 sample.

The charge-transfer resistance (R_{ct}) of the catalyst was evaluated with an equivalent circuit fitting of the Nyquist plot showed in **Figure 4.6d**. The values of R_{ct} are shown in **Table 4.1**. These R_{ct} values showed highest for as-cast ribbon (S0- 1.58 Ω) and minimum for S60 (0.62 Ω). The R_{ct} value reduced with an increase of corrosion time from 0 hr to 1 hr (S30- 0.74 Ω, S45- 0.69 Ω). With further increase in the corrosion time after 1 hr, R_{ct} value again starts increasing (S90- 0.63 Ω, S120- 0.85 Ω) denoting the reduction of the average free route of electrons due to disordered boundary region.

The Nyquist plots obtained here showed a suppressed semi-circle indicating the characteristic response of charge transfer controlled reaction. This OER response is controlled by reaction kinetics and not by diffusion. In addition, kinetically controlled reaction doesn't signify the change in current with the increase of scan rate in cyclic voltammetry. **Fig. S3 (a)** showed CV curves of S60 subjected to varying scan rates. There is no prominent variation in the current density with respect to vertex potentials verified the kinetic control of the OER.

In OER activity, for knowing the actual number of accessible sites participated in the reaction for S60, backward sweep of 500 mV s^{-1} is recorded with the area of 0.00302 V mA as shown in **Fig. S3 (b)**. Number of electrochemically accessible Ni sites are found to be 3.77×10^{16}. TOF for S60 found to be increasing with the increased vertex potential in **Fig. S3 (c)** with a value of 11.63 s^{-1} at 1.75 V (vs RHE).

The same procedure was followed for sample S90 in **Fig. S4 (a-c)**, indicates the area of 0.0023 V mA and 2.87× 10^{16} accessible sites, with a TOF value of 8.1 s^{-1} at 1.75 V (vs RHE). This signifies the better TOF value for S60 indicating the suitability for OER reaction. To evaluate the initiation of the varied OER activity of various surface-modified amorphous ribbons, the ECSA was evaluated by calculation of electrochemical double-layer capacitance (C_{dl}).

Fig. S5 (a-f) indicates the cyclic voltammetry curves recorded for S0, S30, S45, S60, S90 and S120 at varied scan rates of 50, 100, 200, 300 and 500 mV s^{-1}, recorded in non-faradaic potential region in 1 M KOH electrolyte. The S60 showed a higher value of C_{dl} (2.21 mF) than that of S0 (0.07 mF), S30 (1.13 mF), S45 (1.3 mF), S90 (1.3 mF), S120 (1.65 mF) as shown in **Figure 4.6e**. The ECSA values are also presented in **Table 4.1.** This suggests that S60 (55.3 cm^2) provides more active sites for the OER process.

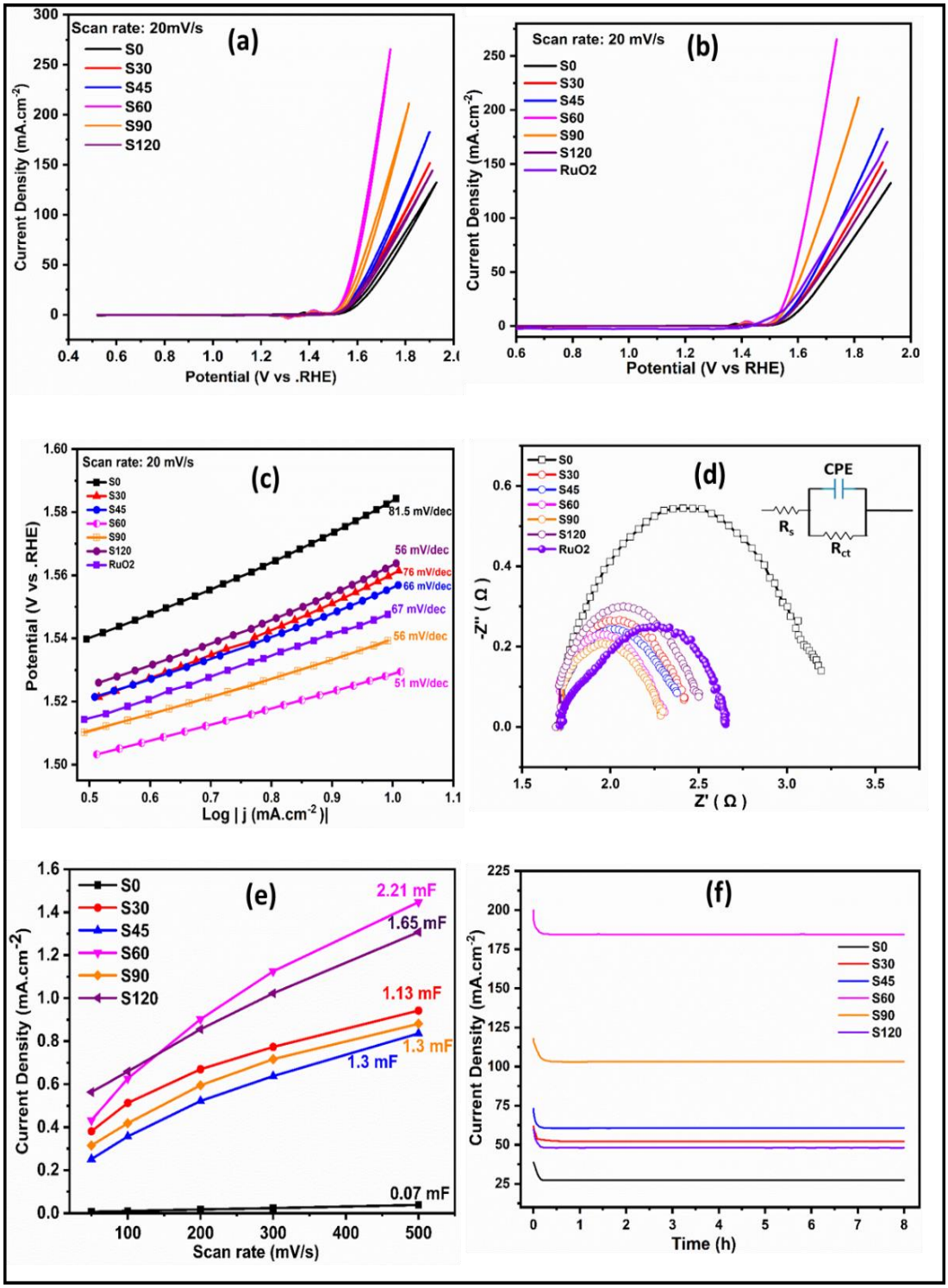

Figure 4.6- Electrochemical characterization of melt-spun and surface modified samples in 1 M KOH (a) Cyclic Voltammetry. (b) Linear polarization. (c) Tafel plots. (d) Nyquist plots. (e) Double layer capacitance (C_{dl}) and (f) Chronoamperometry at 1.7 V (vs RHE).

Long term stability of the catalyst is considered figure of merit for practical application. All modified samples along with melt-spun are subjected to long term stability by chronoameprometry at 1.7 V (vs RHE) subjected to 8 hours **Figure 4.6f.** The surface modified S60 sample showed excellent stability compared other electrodes showing the merit towards OER application [61].

4.5.3.2. Methanol Electro-oxidation

The electrocatalytic oxidation of methanol was evaluated in 1 M KOH in presence of 1 M MeOH recorded vs. Hg/HgO. From the onset potential of methanol oxidation, S90 (1.36 V vs RHE) and S60 (1.38 V vs RHE) showed a better response than other samples (**Figure 4.7a**). However, it is interesting to note from **Figure 4.7b** that S90 and S60 requires lower potential values of (1.38 V vs RHE) and (1.41 V vs RHE) respectively to reach 10 mA/cm^2 with the worst being for S120 (1.43 V vs RHE). It is also interesting to know that S60 sample showed the maximum peak current (275 mA/cm^2) surpassing S90 at 1.54 V vs RHE. Similarly, in **Figure 4.7c**, S90 presented the lowest Tafel slope of 34 $mV\ dec^{-1}$, which was evidently lower than the other samples with S0 (85 $mV\ dec^{-1}$), S30 (77 $mV\ dec^{-1}$), S45 (47 $mV\ dec^{-1}$), S60 (42 $mV\ dec^{-1}$) and S120 (66 $mV\ dec^{-1}$) denoting the faster reaction kinetics. **Figure 4.7d** shows the Nyquist plots with EIS showed the suppressed semi-circle trend. Charge transfer resistance (R_{ct}) of S90 acquired under the similar condition exhibited 0.45 Ω and for melt-spun S0 is 3.45 Ω. This characteristic response showed the charge-transfer controlled reaction in MOR like OER. Also, the electro-oxidation of methanol on S90 surface showed minimum R_{ct} depicting fast charge transfer in Methanol oxidation compared to OER. Catalytic investigations done by Tong et.al on non-noble metal Cu-Ni nanowires showed increased number of NiOOH active sites leading to kinetic controlled MOR [45].

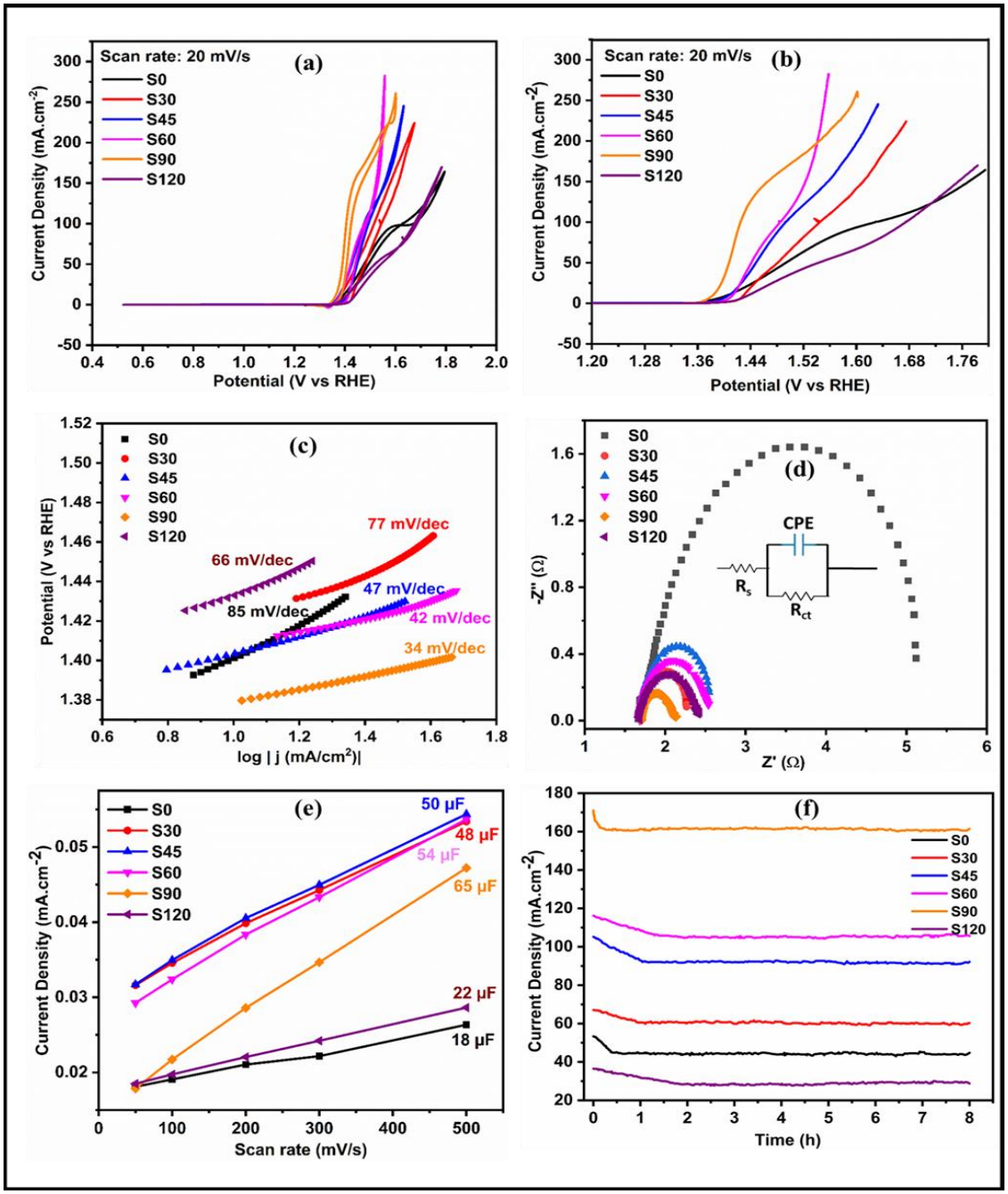

Figure 4.7- Electrochemical characterization of melt-spun and surface modified samples in 1 M KOH+ 1 M MeOH (a) Cyclic Voltammetry. (b) Linear polarization. (c) Tafel plots. (d) Nyquist plots. (e) Double layer capacitance (C_{dl}) and (f) Chronoamperometry at 1.5 V (vs RHE).

Wang et.al showed that NiO/Ni heterostructures developed by thermal annealing procedure, exhibited enhanced increased amount of NiOOH leading to kinetic controlled activity [103].

Fig. S6 (a) showed CV curves of S60 subjected to varying scan rates in 1 M KOH + 1 M MeOH, denoting no remarkable variation in the current density with respect to applied potentials showing the kinetically controlled MOR. To determine the quantity of active accessible sites for MOR with an assumption that only metallic Ni participates in reduction process, backward sweep of 500 mV s^{-1} for S60 is recorded with the area of 0.00343 V mA shown in **Fig. S6 (b)**. Number of electrochemically accessible Ni sites are found to be 4.28×10^{16}. TOF for S60 found to be increasing with the increased vertex potential in **Fig. S6 (c)** with a value of 6.9 s^{-1} at 1.46 V (vs RHE). The same procedure was followed for sample S90 (**Fig. S7 (a-c)**), indicates the area of 0.00335 V mA and 4.18×10^{16} accessible sites, with a TOF value of 7.2 s^{-1} at 1.46 V (vs RHE). It also signifies the better TOF values for S90, even at lower vertex potentials indicating the suitability for MOR reaction.

Figure 4.7e indicates S90 catalyst showed a higher value of C_{dl} (65 µF) than that of S0 (18 µF), S30 (48 µF), S45 (50 µF), S60 (54 µF) and S120 (22 µF). Corresponding CV curves in the non-Faradic region is presented in **Fig. S8 (a-f)**. Electrochemical active surface area (ECSA), an important parameter for electrocatalyst, derived to be S0 (0.45 cm^2), S30 (1.2 cm^2), S45 (1.24 cm^2), S60 (1.35 cm^2), S90 (1.62 cm^2) and S120 (0.56 cm^2) respectively, showing the suitability of S90 for MOR catalysis. All modified samples along with melt-spun are subjected to long term stability by chronoamperometry at 1.5 V (vs RHE) for 8 hours (**Figure 4.7f**). The surface-modified S90 sample showed excellent stability compared S60 showing the merit towards MOR application [104]. In OER, S60 displayed an ECSA value of 55.3 cm^2 in 1M KOH while S90 (31.0 cm^2) showed less

value. In presence of 1M MeOH, S90 showed higher ECSA value (1.62 cm^2) in comparison with S60 (1.35 cm^2). In presence of methanol in KOH, the conductivity of the solution is lowered leading to lower ECSA value compared to 1M KOH. In addition, low surface tension of the methanol containing electrolyte enable the improved contact between the electrolyte and electrodes. Probably, this process enables more access to the active sites in pores present in S90 compared to S60. Thus ECSA of S90 is higher in methanol compared to the S60 leading to better performance of S90 for MOR. Higher ECSA in 1M MeOH supports S90 for early onset potential with sacrificial methanol analyte and afterwards in OER regime, S60 sample showed the superiority.

4.5.3.3. Mechanism

The pristine amorphous ribbon showed a lower electrochemical performance with respect to both OER and MOR. The surface of the as-prepared ribbon is less active due to the lesser accessibility of the active site in the amorphous structure. In the pristine ribbon, the adsorption energy of the reaction intermediates in OER and MOR is less favourable, leading to slower kinetics and delayed onset. In case of surface- modified electrodes, the exposure of active sites is more than the pristine ribbon. It has also been observed in XPS, that surface modified ribbon contains Ni as oxide/hydroxide. It has been reported by many authors that NiOOH is a highly active phase for electrocatalysis [105].

It reduces the adsorption energy of reaction intermediates in OER and MOR. In the case of pristine ribbon, no traces of NiOOH exist leading to the lower efficiency for OER and MOR. Whereas for S60 and S90 samples, the concentration and particle size distribution of α-$Ni(OH)_2$ is optimum resulting in better performance. Also, the presence of low amount of Fe in the precipitated Ni-oxo complex further improves the catalytic activity of the amorphous ribbon [56]. With the lower surface treatment time, the concentration

of NiOOH is lower, resulting in reduced performance. In case of higher treatment time, NiOOH size increases (as stated earlier), leading to lower volume-specific surface area resulting in reduced performance. The selectivity of S90 over S60 for MOR may be explained based on the mechanism of methanol oxidation. Methanol oxidation can take place through two routes: complete oxidation of methanol into CO_2, which is a 6-electron transfer process, and secondly, partial oxidation to formate, which is a 4-electron transfer process [106].

The mechanism can be further classified into two categories: with formation of CO* which leads to the poisoning of catalyst and other one is direct conversion without forming CO*. These two pathways arise due to the different dehydrogenation sites of methanol. Thus, direct dissociation of O-H bonds in methanol leads to the formation of formate and suppresses the formation of CO_2. In the elemental mapping of the deposited α-$Ni(OH)_2$, the concentration of Fe is higher in S90 than in the S60 sample (**Fig. S9** and **Figure 4.4** respectively). The presence of hetero atoms played a crucial role in selectivity. Li et al., 2023 have highlighted the role of Fe/Ni interface in Fe doped $Ni(OH)_2$ [38]. They have highlighted that local aggregates of Fe in $Ni(OH)_2$ modify the electronic distribution near the Fermi-level through electron transfer.

As shown by the same author, the electron transfer takes place from Ni to Fe, leading to a modified d-state of Ni. Also, the presence of Fe and redistribution of electronic state (preferably d-state) near the Fermi level enhances the d-band centre, leading to a rise in antibonding energy [38]. This phenomenon enhances the interaction between the catalytic sites and the intermediates containing oxygen. Higher electron density on oxygen further enhances this interaction in Fe-doped α-$Ni(OH)_2$. In the case of OER and MOR, the initial reactants are OH- and CH_3O^-. Since the CH_3 group has a *+I* effect, it enhances more electron density over oxygen in CH_3O^- as compared to H in OH^- leading to stronger

interaction in MOR [107]. Thus, a higher concentration of Fe in α-$Ni(OH)_2$ enhances the selectivity of S90 for MOR than S60.

A comparison of the present work with the existing literature is shown in **Table 4.2**. Similar performance enhancement was reported by Jang et al, for amorphous ribbon [61]. They have also reported the formation of active site, preferably, oxyhydroxide of nickel, which is responsible for performance enhancement. Whereas, other alloying elements namely Cr, Si and B exhibit lesser active participation in the electrochemical reaction, but tunes the electronic structure of the active sites thereby activating the primary active sites [108]. Since the surface was stable and no reorganization of structure occurred, the performance of the electrocatalyst does not change significantly in terms of LSV in 1 M KOH in absence and presence of 1 M MeOH as shown in **Fig. S10**. Also, the product did not accumulate in the active sites leading to generation of fresh active site every time. This reduces chances of mass transfer limitation. The ribbon used in present study can be prepared in large scale and hence up-scaled for commercial applications.

Fig. S11 indicates the comparison for MOR and OER polarization curves of S90 and S60 samples. Being S60 the best catalyst for OER, performance is shown for MOR also for comparison. Similarly, by looking into suitability of S90 for MOR, performance was shown in OER regime also. It was evident that S60 sample is displaying an over-potential of 295 mV at 10 mA/cm^2 in 1 M KOH compared to the counterpart melt-spun (S0) showing 354 mV. It is also interesting to observe that the S60 showed 10 mA/cm^2 current

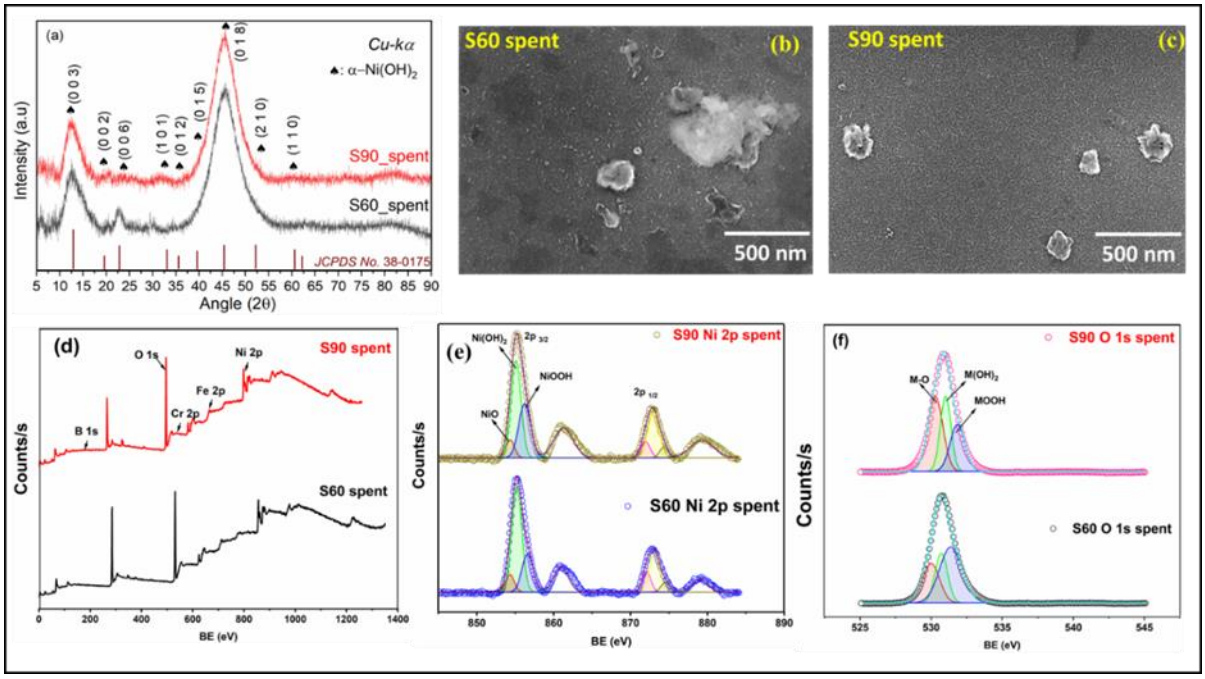

Figure 4.8- Characterization of optimized spent sample (S60 and S90); (a) XRD; (b,c) FE-SEM; XPS spectra (d) surface scan, (e) Core level spectra of Ni 2p and (f) Core level spectra of O 1s.

density at 1.525 V (vs RHE) in 1 M KOH which reduced further to 1.38 V vs RHE in S90 upon addition of 1 M MeOH. As observed in **Figure 4.8a**, the XRD peaks corresponding to α-Ni(OH)2 become more prominent after prolonged performance in both the electrolytes. The XRD of the post-operation optimized sample reveals the presence of pure α-Ni(OH)2 phase of trigonal structure (P-3m1) of space group 162. Further, the order of relative peak intensity and absence of asymmetric broad peaks between (003) and (006) peak indicates stabilization of hydration along the c-axis during electrocatalysis [109].

FE-SEM images in **Figure 4.8b-c** suggest that the granular morphology on the surface of the ribbon becomes more agglomerated as compared to the virgin samples. The surface and core level XPS spectra **Figure 4.8d-f** suggest no significant change in the

composition and complex formation after the prolonged electrochemical study for both S60 and S90 samples. Core level spectra of Ni 2p (Figure **8e**) in S60 and S90 spent sample suggests that the concentration of NiOOH phase is higher in S90 compared to S60 after operation.

4.6. Summary

In summary, we report a free standing Ni based amorphous ribbon $(Ni_{87}Fe_4Cr_9)_{78}Si_8B_{14}$ catalyst by treating the surface through potentiostatic cathodic corrosion for different time intervals (till 120 min), to study the potential application towards eletrocatalytic OER and MOR. This surface treatment leads to formation of α-$Ni(OH)_2$ phase, with varying distribution of nano-sized α-$Ni(OH)_2$ particles over the ribbon surface. Amorphous ribbon with 60 min of surface treatment (S60) has shown optimized OER performance in 1 M KOH and S90 showed the optimized performance for 1 M MeOH in 1 M KOH. The surface treatment of the ribbon catalyst reduced the over-potential as well as charge transfer resistance (R_{ct}) for both OER and MOR. It has been observed that addition of 1 M MeOH in 1 M KOH reduced the applied potential to 1.38 V vs RHE (1.525 V vs RHE in 1 M KOH for S60) in S90 sample to reach 10 mA/cm^2 current density suggesting substitution of OER by MOR in anode, leading to energy efficient hydrogen generation at cathode. Surface treatment resulted in formation of $Ni(OH)_2$ and NiOOH which acts as active sites for electro-oxidation leading to higher efficiency. This surface engineering of the ribbon also helped to develop active catalytic phase of Nickel oxo/hydroxo compounds which enhanced the efficiency towards OER and MOR and showed applicability in DMFC and hydrogen generation.

Table 4.1- OER Parameters of potentially etched samples ([a] Current density considered in this case is 10 mA cm^{-2})

Sample	**Over-potential[a] (mV)**	**Tafel slope (mV dec^{-1})**	**Rct (Ω)**	**$ECSA_{OER}$ (cm^2)**
S0	354	81.5	1.58	1.8
S30	329	76	0.74	28.4
S45	325	66	0.69	31.9
S60	295	51	0.62	55.3
S90	309	56	0.63	31.0
S120	334	56	0.85	41.4

Table 4.2- OER comparison with reported transition metal based electrodes in KOH. Current density considered in this case is 10 mA cm^{-2}.

Catalyst	Phase	η (mV)	Tafel slope (mV/dec)	Electrolyte	References
$(Ni_{87}Fe_4Cr_9)_{78}Si_8B_{14}$ – S60	Amo	**295**	**51**	**1 M KOH**	**This work**
$(Ni_{87}Fe_4Cr_9)_{78}Si_8B_{14}$ – S90	Amo	**309**	**56**	**1 M KOH**	**This work**
np-$Fe_{40}Ni_{37}Nb_3P_{13}C_7$	Amo	276	35.9	1 M KOH	[68]
FeCoCrNi	Cryst.	300	51.4	1 M KOH	[110]
NiPdP	Cryst.	340	46	1 M KOH	[111]
FeCoNiB	Amo	274	38	1 M KOH	[112]
NiFeB	Amo	319	56	1 M KOH	[113]
$Ni_{50}Fe_{25}B_{15}Si_7P_3$	Amo	306	45.1	1 M KOH	[61]
$Fe_{25}Co_{25}Ni_{25}Mo_9P_8B_8$	Amo	281	36.44	1 M KOH	[63]
$Ni_{50}Fe_{25}B_{15}Si_7P_3$	Amo	269	40.5	1 M KOH	[61]
np-NiFeMoP	Amo	197	41.2	1 M KOH	[62]
$Fe_{78}Si_9B_{13}$	Amo	356	45	1 M KOH	[65]
Amo= Amorphous ; Cryst. = crystalline ; np = nano-porous					